INTERNATIONAL JOURNAL OF ENERGY STUDIES

e-ISSN: 2717-7513 (ONLINE); homepage: https://dergipark.org.tr/en/pub/ijes

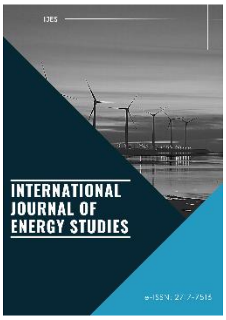

Research Article

Int J Energy Studies 2026; 11(1): 587-611

DOI: 10.58559/ijes.1865873

Received	:	17 Jan 2026
Revised	:	16 Feb 2026
Accepted	:	23 Feb 2026

Effect of biomimetic fish forms on minibus aerodynamics: CFD and wind tunnel comparison

Erman Doğan[a], **Seda Kırmacı Arabacı**[b*]

[a]*Department of Mechanical Engineering, Manisa Celal Bayar University, Manisa, Türkiye, e-mail: doganerman35@gmail.com, ORCID: 0000-0003-3739-7470*

[b]*Department of Mechanical Engineering, Manisa Celal Bayar University, Manisa, Türkiye, ORCID: 0000-0001-8903-5952*

*(*Corresponding Author:seda.kirmaci@cbu.edu.tr)*

Highlights

- Biomimetic minibus designs inspired by aquatic species were developed and analyzed.
- Humphead wrasse-based geometry achieved a 16.03% reduction in drag coefficient.
- CFD results were validated by wind tunnel tests on a 1:28 scale prototype.
- Drag reduction enables ~8% fuel savings and significant CO_2 emission reduction.

You can cite this article as: Doğan E, Arabacı SK. Effect of biomimetic fish forms on minibus aerodynamics: CFD and wind tunnel comparison. Int J Energy Studies 2026; 11(1): 587-611.

ABSTRACT

This research explores the aerodynamic benefits of incorporating biomimetic design principles into commercial minibus bodies by mimicking the cranial morphology of select aquatic species. Inspired by the pronounced head structures and maneuverability of the hump head wrasse, green hump head parrotfish, and flowerhorn fish, three alternative vehicle geometries were developed and compared to a conventional reference model. Computational fluid dynamics (CFD) analyses were performed using the k–ω SST turbulence model, and experimental validation was conducted via wind tunnel testing on a 1:28 scale prototype. Among the configurations, the hump head wrasse-based model exhibited the most favorable aerodynamic behavior, achieving a 16.03% reduction in drag coefficient relative to the baseline. This improvement corresponds to an estimated 8% decrease in fuel consumption, translating to approximately 324 liters of annual savings for a vehicle operating over 45,000 km, and a projected reduction of 748 kg of CO_2 emissions. The results demonstrate that biologically derived shapes can contribute meaningfully to the aerodynamic refinement of ground vehicles, with direct implications for environmental sustainability and energy efficiency.

Keywords: Biomimetic vehicle design, Minibus aerodynamics, CFD simulation, Wind tunnel testing, Drag reduction

1. INTRODUCTION

All living organisms exhibit morphological and functional traits shaped by their ecological context and environmental constraints [1]. These biological adaptations have continually informed engineering practices, offering natural templates for efficient and sustainable design strategies [2,3]. Biomimetics, which integrates biological insights into engineering challenges, has led to domain-specific advancements ranging from fluid dynamics to structural optimization. Examples include the Airbus Bird of Prey project, which emulates eagle wing and tail dynamics to improve flight control [4], and the Shinkansen E5 bullet train, whose aerodynamic design was inspired by the beak of a kingfisher to reduce noise pollution [7]. Architectural and product designs, such as the Eastgate Building in Zimbabwe modeled after termite mounds [8], and Sharkskin-textured swimsuits, developed to minimize hydrodynamic resistance, underscore how biomimetic solutions transcend disciplinary boundaries [9-10]. In fluid mechanics, the interaction between organisms and surrounding fluids has shaped evolutionary developments in both structure and behavior [23]. For example, the scale arrays of fish reduce drag, and similar textures are being applied to vehicles and aircraft [5,6]. Likewise, the tubercles found on the fins of humpback whales help stabilize flow and reduce drag and have been successfully adapted in wind turbine blades and airplane wings [12]. Evolution has refined such traits over millennia, offering nature-validated frameworks for enhancing aerodynamic performance. Biomimetic approaches have found increasing relevance in vehicle aerodynamics, particularly in the context of rising fuel costs, stricter emission standards, and the need to extend electric vehicle range. Studies report that aerodynamic drag accounts for up to 80% of total energy loss in ground vehicles traveling over 80 km/h highlighting the critical role of aerodynamic drag reduction in lowering energy losses and meeting environmental regulations [41]. As of 2020, European regulations limit CO_2 emissions to 95 g/km, down from 120 g/km in 2012, pressuring manufacturers to optimize vehicle designs [40]. A wide range of bioinspired designs has been investigated in automotive engineering. The Mercedes-Benz Bionic Car, based on the boxfish, demonstrated a drag coefficient (Cd) of 0.19, resulting in 35% fuel savings compared to conventional models [13,14]. Studies on boxfish also revealed that despite its angular body shape, it achieves low drag, with Cd values as low as 0.073 at 100 km/h, and biomimetic applications based on its form have achieved up to 66.5% drag reduction [22,52]. Vehicle surface designs influenced by marine species like the beluga whale and sea lion have demonstrated notable aerodynamic gains, achieving drag reductions of 12.6% and 20%, respectively, under controlled conditions [16,18,65]. Sareh emphasizes that contemporary bioinspired vehicle development increasingly relies on numerical optimization tools to translate natural morphologies into quantifiable aerodynamic improvements. This perspective aligns with the present study, where fish-inspired geometries were systematically abstracted and evaluated through CFD-based numerical analysis [67]. Ground vehicle designs have also been enhanced through biomimetic strategies, particularly in efforts to balance aerodynamic refinement with structural functionality. Tiger beetles, cobras, and even felines have influenced design strategies aimed at balancing aerodynamic performance and structural efficiency [1,15]. In particular studies focusing on wrasses and parrotfish—species known for their maneuverability and streamlined shapes—indicate that their body forms evolved to meet complex functional demands driven by environmental flow conditions [24–34]. Insights into these morphological features offer practical guidance in configuring vehicle geometries suited for turbulent flow regimes. Aerodynamic enhancements have been systematically evaluated through a combination of experimental measurements and validated computational simulations. Modifying bus geometries has led to 14% drag reduction and 8.4% lower fuel consumption [36], while rear-mounted expanders, diffusers, and shrouds have yielded drag decreases of 8.2% to 59% in various vehicle types [54–58]. In buses, aerodynamic devices have achieved up to 8.6% improvement, and for sedans, rear wind breaks reduced drag by 1.7%, although diffuser angle changes beyond certain thresholds increased drag [39]. CFD predictions, when compared to wind tunnel measurements, generally exhibit deviation margins below 4%, indicating reliable correlation between numerical and physical results [37]. Other small but effective adjustments—such as mirror placement or windshield angle can further reduce drag by 2–3% [38,53]. While significant progress has been made, the challenge of transferring biologically inspired shapes into practical vehicle designs remains complex. Nature has addressed these aerodynamic problems over 600 million years through iterative adaptation and refinement [42]. Thus, biomimetic forms particularly from aquatic organisms, offer untapped potential for further reducing aerodynamic resistance in ground vehicles. Shams Taleghani and Torabi highlighted how contemporary aerodynamic studies increasingly integrate high-fidelity numerical simulations with experimental validation to enhance performance prediction accuracy. These developments support the methodological framework adopted in the present study, where CFD analysis is coupled with wind tunnel testing to ensure reliable aerodynamic assessment [66]. This study aims to explore how the distinctive cranial morphologies and agile body structures of certain fish species can be adapted to optimize the aerodynamic performance of commercial minibuses and to reduce the aerodynamic drag force. The study examines the aerodynamic implications of integrating fish-inspired forms into minibus design, focusing on how morphological features can influence flow behavior. These fish were chosen because of their large head structure and high maneuverability. The incorporation of such biomimetic head profiles is expected to enhance fuel economy by reducing aerodynamic resistance under highway driving conditions. Such aerodynamic improvements have the potential to lower fuel consumption and associated CO_2 emissions, contributing to more sustainable transportation practices. In electric vehicles, the range will be increased. These outcomes align with broader environmental objectives, including the shift toward a low-carbon economy and the advancement of sustainable development targets.

2. BIOINSPIRED DESIGN PROCESS

This study focused on three aquatic species humphead wrasse, green humphead parrotfish, and flowerhorn fish, chosen due to their pronounced cranial features and exceptional navigational agility in fluid environments. The cranial protrusions of these species were analyzed not only in terms of visual distinctiveness but also for their potential to favorably influence flow separation and surface pressure distribution. 3D geometries highlighting the cranial volumes were developed and scaled to maintain equivalence in frontal area and overall body volume with the baseline minibus model for consistent aerodynamic comparison These biological profiles were abstracted into manufacturable geometries suitable for CFD analysis, enabling evaluation under controlled aerodynamic conditions. The bioinspired design approach is illustrated in Figure 1.

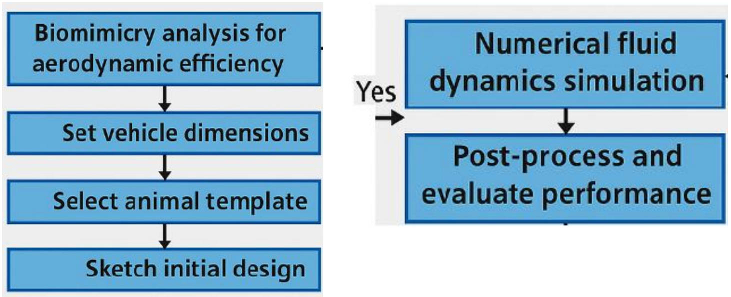

Figure 1. A nature-inspired vehicle form development approach via CFD simulation

2.1. Modeling of High-Maneuverability Fish Species for Biomimetic Design

The selected fish species were characterized by pronounced cranial protrusions and exceptional fluid maneuverability, making them ideal biological analogs for aerodynamic form exploration. For these reasons, the humphead wrasse, green humphead parrotfish, and flowerhorn fish were prioritized in this study. These head bulges are hypothesized to modulate surface pressure gradients and promote delayed flow detachment, contributing to reduced aerodynamic resistance.

Informed by these morphological traits, three-dimensional vehicle bodies were digitally modeled in Solidworks, ensuring accurate translation of biological profiles into engineered surfaces. The humphead wrasse (Figure 2(a)), one of the largest members of the Labridae family,, can reach up to 2 m in length and 190 kg in weight [43–46]. The green humphead parrotfish (Figure 2(b) frequently inhabiting turbulent reef zones, exhibits agile directional control and dynamic postural adjustment under variable flow conditions [47,48]. The third model, based on the flowerhorn fish, originates from South America and was developed in Malaysia and Thailand in the 1990s (Figure 2(c)). This species typically reaches up to 40 cm in length and features a rounded, bilaterally symmetrical form, suitable for representing reduced-scale aerodynamic curvature [49,50]. The morphologies extracted from the selected fish species were geometrically scaled and embedded into vehicle body designs, which were then analyzed via computational aerodynamic simulations. The objective was to systematically reinterpret biological forms into manufacturable and aerodynamically viable geometries applicable to commercial minibus configurations.

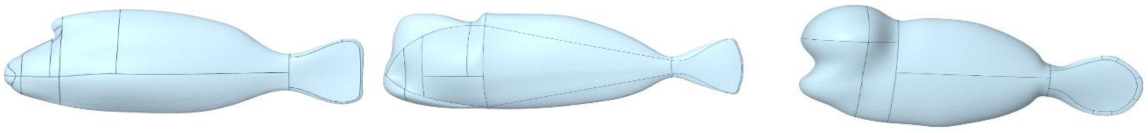

(a) (b) (c)

Figure 2. 3D models of fishes (a) humphead wrasse fish design (b) green humphead parrotfish design (c) Flowerhorn fish design

3. METHODOLOGY

The aerodynamic characteristics of the biomimetic minibus models were evaluated through an integrated approach combining CFD simulations and wind tunnel testing. The biologically derived vehicle forms were systematically compared with a conventional reference design under identical geometric and boundary conditions to ensure fairness in aerodynamic evaluation. The process involved 3D modeling, CFD simulations using the k-ω SST model, and wind tunnel testing of the most effective design. Validation against experimental measurements enabled a robust assessment of the aerodynamic efficacy of the proposed biomimetic geometries within practical design constraints.

3.1. Determination of the Models Used in Minibus Design

Four distinct minibus configurations were developed for comparative aerodynamic assessment, including one conventional and three biomimetically inspired variants. The baseline model, designated as T1, was geometrically derived from the long-wheelbase version of the Mercedes Sprinter 316, serving as a commercially available benchmark.

The remaining three models T2, T3, and T4 were inspired by the body forms of the humphead wrasse, green humphead parrotfish, and flowerhorn fish, respectively. To ensure comparability, each model retained uniform exterior dimensions 6.961 m (L), 2.610 m (H), and 2.426 m (W) with a standardized ground clearance of 1.96 m. The frontal projected areas of all models were held constant at 2.4 m^2 to eliminate geometric bias in drag computation. Holding these dimensional parameters constant ensured that observed variations in aerodynamic performance could be attributed exclusively to differences in outer body contour. According to manufacturer data, the reported drag coefficient of the original Mercedes Sprinter 316 model is approximately 0.32 [51]. The technical specifications of the Mercedes Sprinter 316 are shown in Figure 3(a), while the corresponding 3D reference model (T1) is illustrated in Figures 3(b) and 3(c). The biomimetic models are visualized as follows: the T2 model, inspired by the humphead wrasse, appears in Figure 4(a); the T3 model, derived from the green humphead parrotfish, is presented in Figure 4(b); and the T4 model, developed from the flowerhorn fish, is shown in Figure 4(c). All models were designed to maintain equal volume and frontal area, enabling fair and consistent comparison across designs.

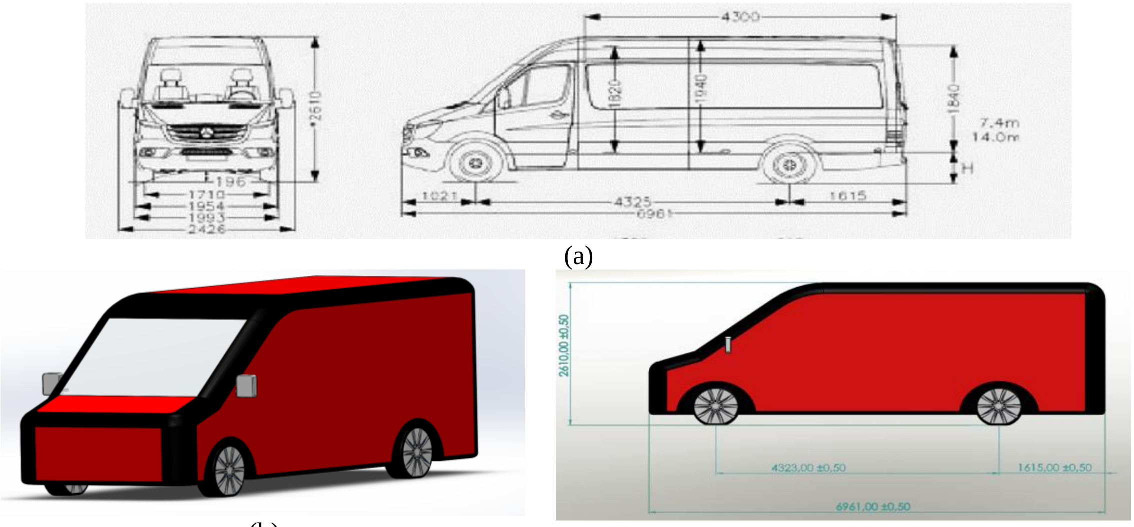

(a)

(b)

(c)

Figure 3. (a) Technical specifications of the Mercedes Sprinter model; (b–c) 3D design of the Mercedes Sprinter 316-based reference model (T1)

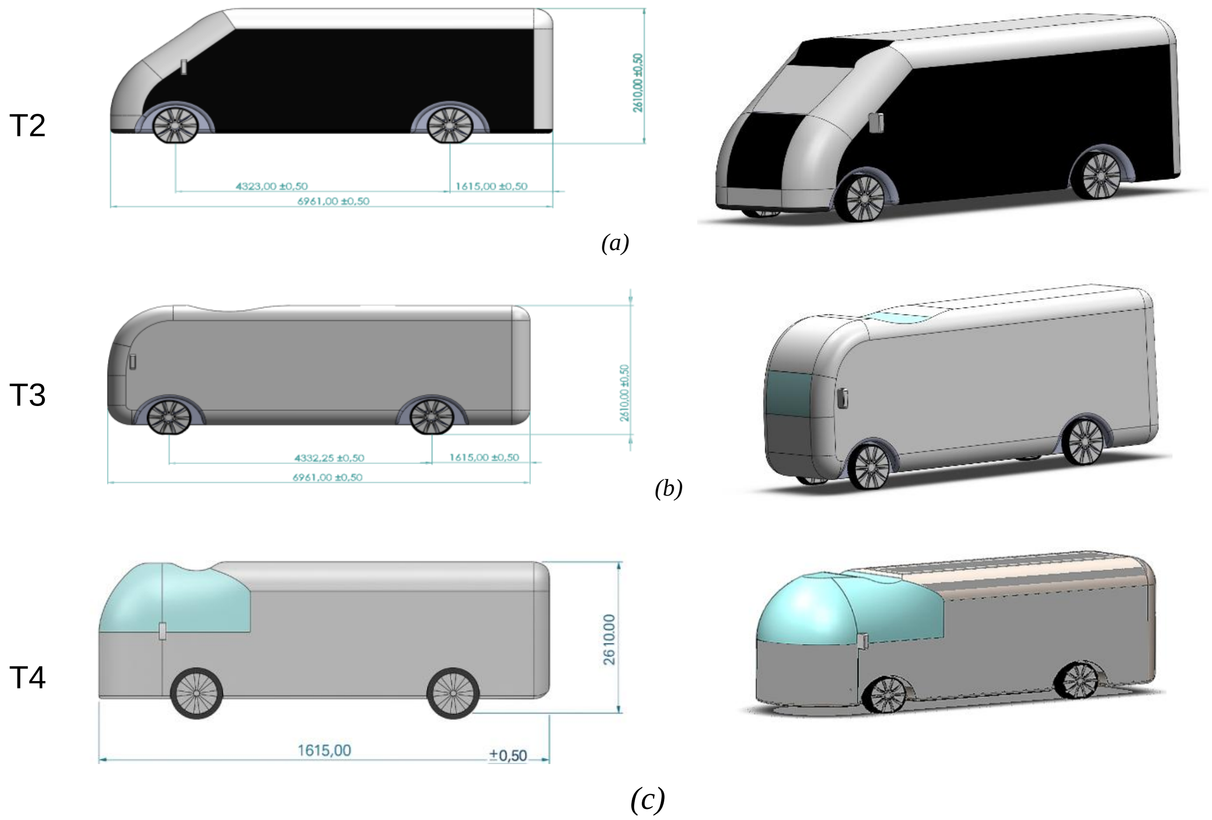

Figure 4. (a) T2 model inspired by the humphead wrasse; (b) T3 model based on the green humphead parrotfish; (c) T4 model developed from the flowerhorn fish

3.2. Computational Methods

The aerodynamic performance of the minibus models was evaluated using steady-state CFD simulations in ANSYS Fluent at different flow velocities. The k–ω SST turbulence model was selected due to its superior performance in resolving near-wall gradients and accurately capturing adverse pressure gradient-induced flow separation [16,22]. In this study, the Shear Stress Transport (SST) based k–ω turbulence model was employed for turbulence modelling. The SST model combines the advantages of the standard k–ε and k–ω models and is particularly effective in predicting boundary layer separation. The model consists of two transport equations: one for the turbulent kinetic energy (k) and another for the specific dissipation rate (ω). Additional terms for production and diffusion, as well as the definition of turbulent eddy viscosity, close the system. The eddy viscosity formulation includes a limiter function to prevent excessive growth of the production term, enhancing numerical stability in high-gradient flow regions. Numerical simulations were performed using the SST model as implemented in Fluent, with fine mesh resolution ensuring low y^+ values near the wall. Due to its hybrid nature, where the model behaves like k–ω near walls and transitions to k–ε in the free stream, accurate predictions were achieved in separation and recirculation zones. The two-equation model is as follows [33]:

$$\partial(\rho k)/\partial t + \partial(\rho u_j k)/\partial x_j = P - \beta\rho\omega k + \partial/\partial x_j \, [\, (\mu + \sigma_k \, (\rho k/\omega)) \, \partial k/\partial x_j \,] \tag{1}$$

$$\partial(\rho\omega)/\partial t + \partial(\rho u_j \omega)/\partial x_j = (\gamma\omega/k)P - \beta\rho\omega^2 + \partial/\partial x_j \, [\, (\mu + \sigma_k \, (\rho k/\omega)) \, \partial k/\partial x_j \,] + (\rho\sigma_d/\omega) \, \partial k/\partial x_j \, \partial\omega/\partial x_j \tag{2}$$

$$P = \tau_{ij} \, \partial u_i/\partial x_j \tag{3}$$

$$\tau_{ij} = \mu_t \, (2S_{ij} - (2/3) \, \partial\mu k/\partial xk \, \delta_{ij}) - (2/3) \, \rho k \, \delta_{ij} \tag{4}$$

$$S_{ij} = (1/2) \, (\partial u_x/\partial x_j + \partial u_j/\partial x_i) \tag{5}$$

The PISO algorithm was utilized for pressure–velocity coupling, while second-order discretization schemes ensured higher accuracy for momentum transport, turbulence closure, and pressure interpolation. Spatial gradients were computed using the Green–Gauss node-based approach, which offers reliable estimation of scalar variations across control volumes [59,60]. The mesh consisted of tetrahedral and prism elements. Wall-adjacent flow regions were treated using enhanced wall functions, with the first cell height calibrated to achieve $y^+ \approx 1$, thereby enabling accurate boundary layer resolution without excessive mesh refinement.

3.2.1. Numerical simulations

Each vehicle geometry was embedded within a computational domain defined as a rectangular control volume, carefully dimensioned to ensure unimpeded flow development upstream, downstream, and laterally The computational boundaries were placed at distances of 2 vehicle lengths upstream and overhead, and 5 lengths downstream, to mitigate boundary-induced flow artifacts and ensure domain independence. Owing to the lateral geometric symmetry of the vehicle designs, only half of each configuration was simulated, employing a mid-plane symmetry condition to reduce computational load (Figure 5).

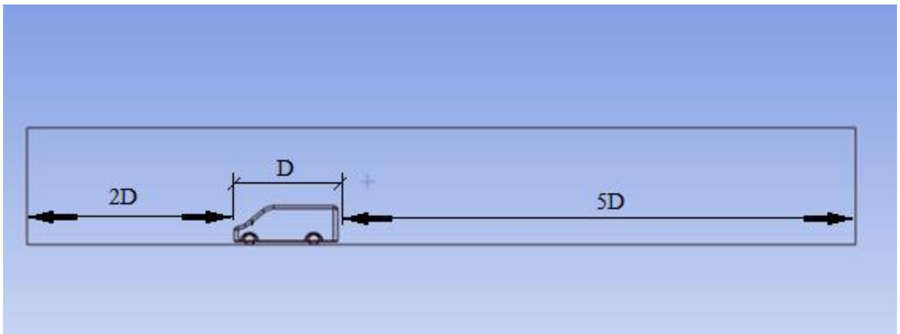

Figure 5. Control volume in the half-model CFD simulations

3.2.2. Mesh independence

A mesh independence analysis was conducted on the baseline model (T1) at 100 km/h (27.7 m/s) to quantify discretization effects and ensure numerical consistency. Different mesh densities were tested while keeping all boundary conditions and turbulence models constant. Convergence of the drag coefficient was observed beyond a mesh resolution of 3.33 million cells and 623,825 nodes, indicating mesh sufficiency for the given flow regime. Accordingly, the identified mesh resolution was adopted for all vehicle configurations to maintain consistency in numerical comparison. Mesh quality metrics yielded an average skewness of 0.20 and an orthogonal quality of 0.79, both within acceptable CFD standards, confirming mesh reliability. A visual representation of the mesh is shown in Figure 6.

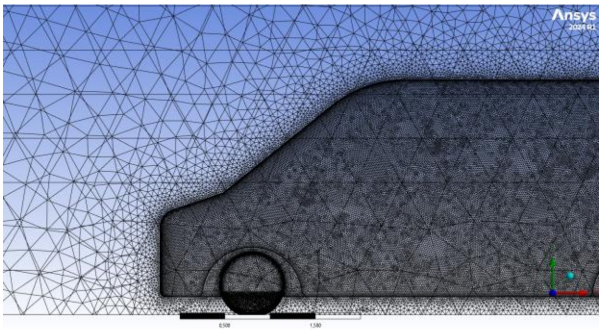

Figure 6. Mesh of minibus

Six progressively refined grids were tested on the T1 model at 100 km/h to determine the point of grid convergence for aerodynamic parameters. With 3,329,970 cells, the Cd stabilized at 0.403, and further refinement yielded no significant change. This mesh was used for all models. The convergence curve is shown in Figure 7.

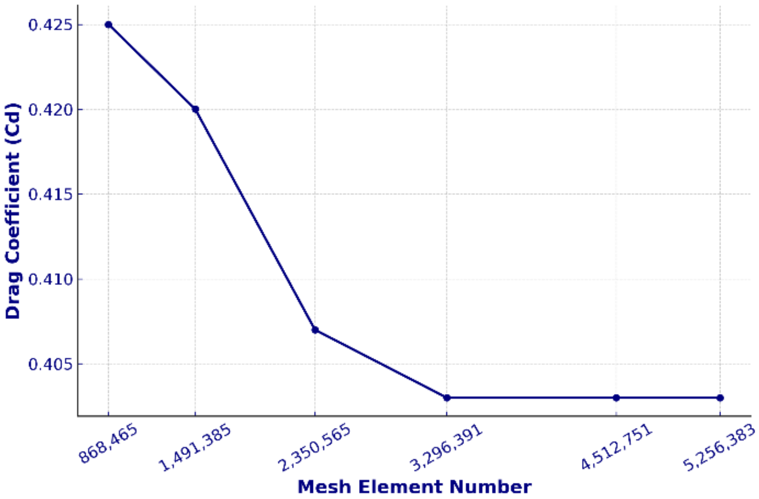

Figure 7. Mesh convergence study

3.2.3. Boundary conditions and Near-Wall Modeling

Simulations were conducted at three inlet velocities 16.6, 27.7, and 33.3 m/s representative of low to moderate driving conditions for commercial vehicles. The outlet was set to 0 Pa as reference pressure. The vehicle surface and ground were assigned no-slip conditions, while the ground was further modeled as a moving wall to replicate relative motion between road and vehicle. To minimize boundary layer development at domain limits, free-slip conditions were imposed along the lateral and upper boundaries. Owing to geometric symmetry along the longitudinal plane, simulations were performed on half-domain configurations with a symmetry boundary applied at the centerline. Ambient flow conditions were specified as 15.5 °C air temperature, 1.225 kg/m^3 density, and dynamic viscosity of 1.79×10^{-5} kg/(m·s), reflecting standard sea-level atmospheric conditions. A turbulence intensity of 2% and turbulent viscosity ratio of 5 were prescribed at the inlet, aligning with typical external flow assumptions for vehicle aerodynamics. The k-ω SST turbulence model was used. For reference, the turbulence intensity at the inlet may also be estimated via empirical correlation as (6), providing a Reynolds number-dependent approximation suitable for external aerodynamic simulations.

I= 0,16.(Re)-1/8 (6)

A locally refined boundary layer mesh was employed with a first-cell thickness of ~0.0003 mm, calibrated to maintain $y^+ \approx 1$ for accurate capture of viscous sublayer phenomena. Although the overall flow was in the high Reynolds number regime, a low-Re mesh approach was used near the wall, enabling detailed resolution of the viscous sublayer, buffer region, and turbulent core. The transition from laminar to turbulent flow was considered, and relevant subregions were modeled accordingly [62]. This setup was compatible with the k-ω SST turbulence model, and wall functions were activated to ensure numerical stability. The wall-adjacent cell height was estimated using Equations (7)–(10), based on the empirical skin friction coefficient (Cf), wall shear stress (τ), friction velocity (U*), and the first cell height value.

$$C_f = 0.058\,Re^{-0.2} \tag{7}$$

$$\tau_w = 0.5\rho C_f V^2 \tag{8}$$

$$U^* = \sqrt{\frac{\tau_w}{\rho}} \tag{9}$$

$$y = \frac{y^+\mu}{U^*\rho} \tag{10}$$

4. RESULTS AND DISCUSSIONS

4.1. Drag Coefficient and Drag Force Comparison of Minibus Models at Constant Speed

To isolate the effects of body contour on aerodynamic performance, all minibus models were assessed under equivalent flow velocities, frontal areas, and volumetric dimensions. According to the numerical results summarized in Table 1, the baseline configuration (T1) produced a drag coefficient of 0.368, corresponding to a drag force of 855.48 N at a velocity of 27.7 m/s. Among all tested variants, the T2 configuration demonstrated the most favorable aerodynamic behavior, reducing the drag coefficient and drag force by 16.03% and 15.7%, respectively, relative to the reference The T3 and T4 designs yielded moderate aerodynamic improvements, with drag coefficient reductions of 10.3% and 3.3%, and drag force reductions of 8.4% and 4.1%, respectively. These findings affirm the aerodynamic superiority of the T2 configuration, derived from the humphead wrasse morphology, which consistently outperformed alternative geometries across all evaluated metrics.

Table 1. CFD-Based Drag Coefficient and Drag Force Values of Equal-Volume Minibus Models at 27.7 m/s

Model	**C_d**	**ΔC_d (%)**	**F_d (N)**	**ΔF_d (%)**
T1(Ref Mod.)	0.368	–	855.48	–
T2	0.309	↓16.03%	721.22	↓ 15.7 %
T3	0.330	↓ 10.3 %	783.90	↓ 8.4 %
T4	0.356	↓ 3.3 %	820.66	↓ 4.1 %

The results indicate that even localized changes in frontal geometry can lead to meaningful improvements in aerodynamic performance. The superior outcome of the T2 model demonstrates the feasibility of integrating naturally evolved forms into engineering design. The comparative distribution of drag coefficient values is presented in Figure 8(a), while the corresponding drag force results are illustrated in Figure 8(b).

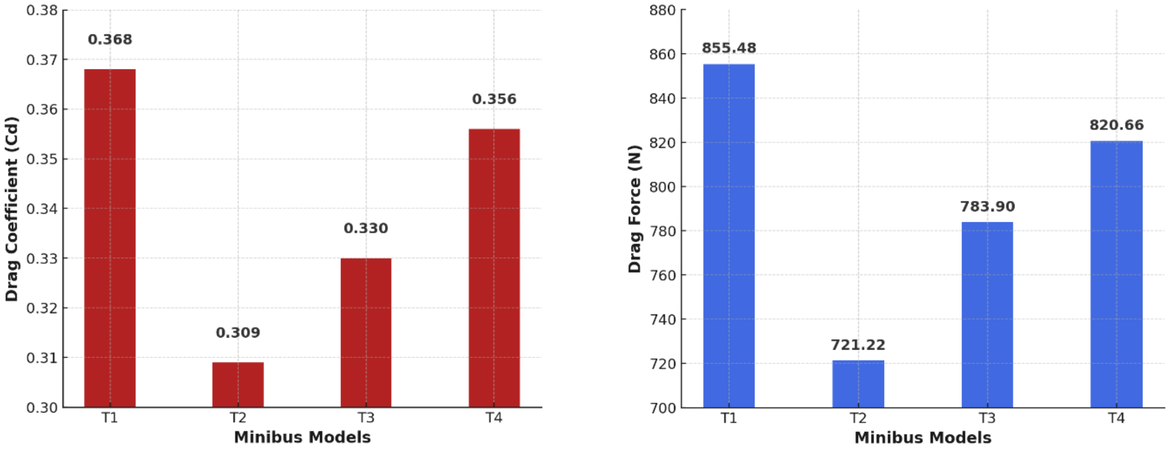

Figure 8. (a) Drag coefficient and (b) Drag forces of minibus models at 27.7 m/s

4.2. Velocity-Dependent Aerodynamic Behavior of the Optimal Design

The aerodynamic behavior of the minibus designs was assessed at inlet velocities of 16.6, 27.7, and 33.3 m/s, yielding approximate Reynolds numbers of 6.41×10^6, 1.05×10^7, and 1.28×10^7, respectively. The variation of drag coefficients and drag forces are illustrated in Table 4.2. The results presented in Table 2 correspond to all minibus models without side mirrors. To quantify the aerodynamic influence of external attachments, supplementary CFD simulations were performed on the T1 model with and without side mirrors. At a velocity of 27.7 m/s, the drag force for the full T1 model (with mirrors) was measured as 855.48 N, whereas the symmetry-based mirrorless version yielded 427.74 N, resulting in a difference of 47.34 N attributable to the presence of side mirrors. Similarly, the drag coefficient was determined to be 0.368 for the full model. The presence of side mirrors led to an increase of 0.032 in drag coefficient—equivalent to an 8.7% aerodynamic penalty—highlighting their non-negligible contribution to overall resistance. With rising velocity, all configurations demonstrated a consistent decline in drag coefficient, indicative of Reynolds number-dependent boundary layer stabilization (Figure 9). For example, the reference model T1 showed a reduction from 0.380 to 0.362, while the T2 model (inspired by the humphead wrasse) decreased from 0.326 to 0.303 over the same velocity range. Across the evaluated Reynolds number range, the T2 model persistently exhibited the lowest drag coefficients, confirming its robustness in varying flow regimes. Compared to T1, the T2 configuration achieved Cd reductions of 14.2%, 16.0%, and 16.3% at 16.6, 27.7, and 33.3 m/s, respectively demonstrating increasing aerodynamic gains with velocity. These improvements indicate that the aerodynamic efficiency of the biomimetic design becomes more pronounced at higher Reynolds numbers. The T3 model offered up to 10.3% improvement, while the T4 model provided only about 3.6%.

These results confirm that the bulging frontal geometry of the T2 model effectively delays flow separation and reduces pressure drag, enabling smoother and more efficient flow along the minibus body.

Table 2. Drag coefficients and drag forces at different velocities

	C_d at 16.6 m/s	C_d at 27.7 m/s	C_d at 33.3 m/s	F_d at 16.6 m/s (N)	F_d at 27.7 m/s (N)	F_d at 33.3 m/s (N)
T1 (Ref.)	0.380	0.368	0.362	307.94	855.48	1121.94
T2	0.326	0.309	0.303	263.90	721.22	1005.84
T3	0.348	0.330	0.327	281.98	783.90	1082.28
T4	0.367	0.356	0.349	303.86	820.66	1162.44

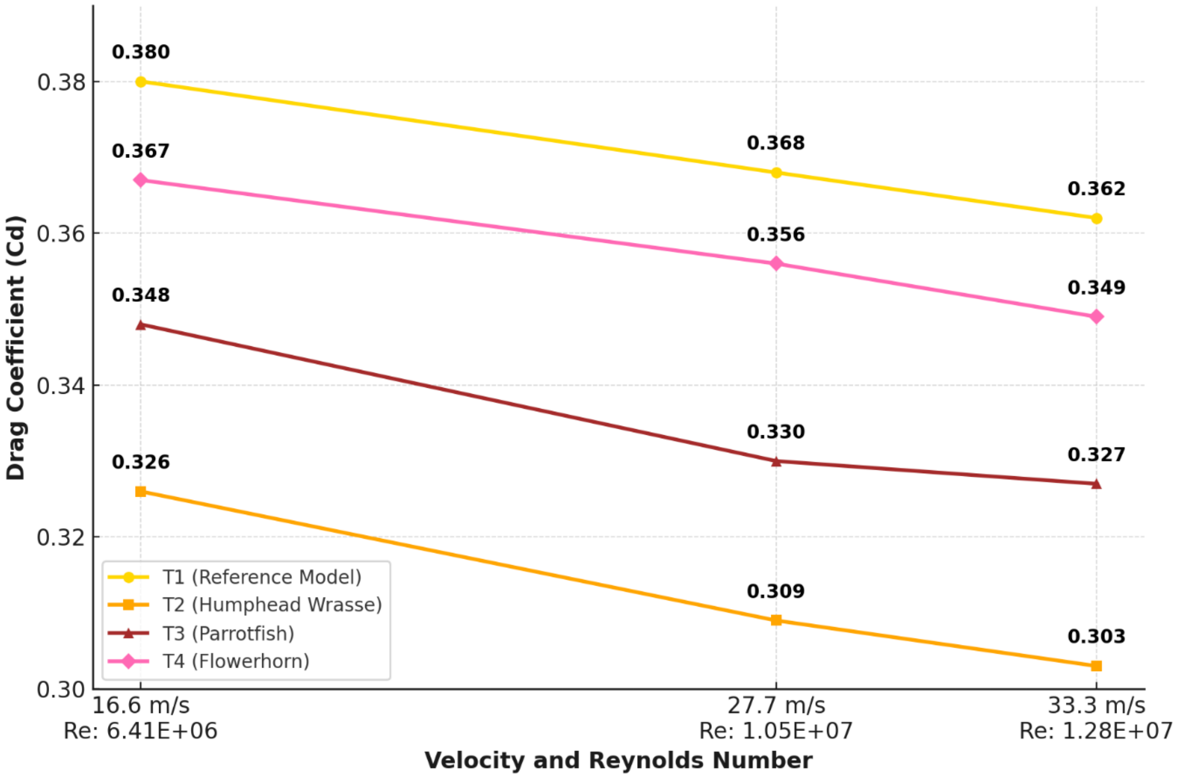

Figure 9. Drag coefficients variation with Velocities and Reynolds numbers for all models

Figure 10 presents the variation of drag force Fd for all minibus models at three different speed 16.6 m/s, 27.7 m/s, and 33.3 m/s—corresponding to Reynolds numbers of approximately 6.41×10^6, 1.05×10^7, and 1.28×10^7, respectively. As expected, the drag force increased with the square of velocity. However, the rate of increase varied among the models. Notably, the biomimetic designs, particularly T2, exhibited a more controlled rise in drag force. For instance, the drag force of the reference model T1 increased from 307.94 N to 1121.94 N, while the T2 model increased more modestly from 263.90 N to 1005.84 N across the same velocity range. This highlights the superior aerodynamic efficiency of the T2 design, even at higher speeds. The improvement percentages of T2 over T1 in terms of drag force are as follows: 14.3% at 16.6 m/s, 15.7% at 27.7 m/s, 10.4% at 33.3 m/s. The T3 model showed moderate improvement (about 8–9%), while T4 exhibited minimal gains (1.3–4.7%).

These results confirm that the flow-guiding frontal structure of the T2 model effectively reduces overall aerodynamic resistance not just the coefficient of drag. This is particularly valuable in commercial minibuses, where such reductions can significantly improve fuel economy and lower emissions.

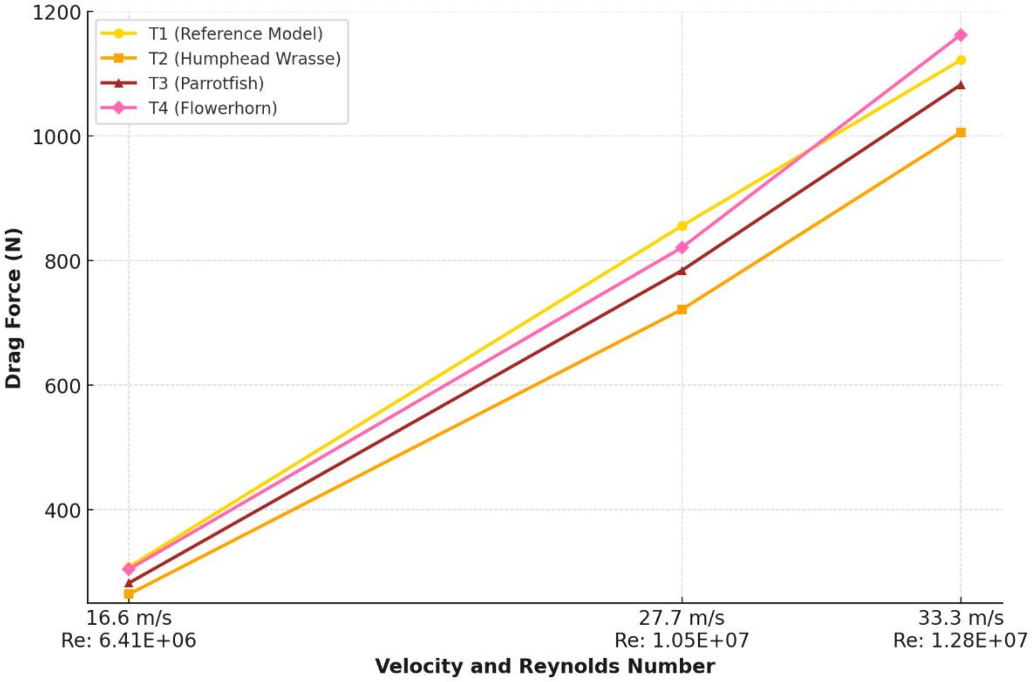

Figure 10. Drag forces variation with velocity and Reynolds number

4.3. Pressure and Streamline Distributions for All Minibus Models

Figure 11 illustrates the static pressure fields on the frontal surfaces of all four minibus configurations (T1–T4) under a 27.7 m/s freestream velocity. The pressure scale is fixed between +494 Pa and –1500 Pa. Owing to its blunt frontal profile, the T1 model exhibits an extensive high-pressure stagnation zone at the front, which significantly contributes to increased form drag. In contrast, the T2 model, inspired by biological morphology, generates a more gradual frontal pressure transition, effectively minimizing stagnation effects. The curvature transitions near the roofline and lateral edges in T2 promote favorable flow redirection, reducing adverse pressure buildup and mitigating local separation. This indicates that T2 features a more aerodynamically refined front geometry. The steeper pressure gradients observed in T3 and T4 near the frontal edges imply earlier deceleration and inferior flow attachment relative to T2. Among all geometries, T2 delivers the most aerodynamically optimized frontal pressure topology, directly correlating with its superior drag reduction performance.

These results are consistent with the drag coefficient reductions discussed in the following sections.

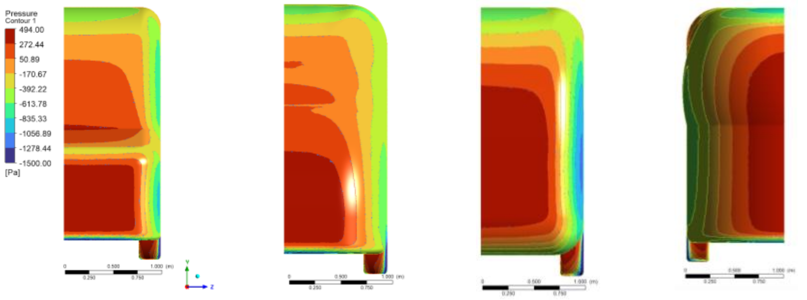

(a) **(b)** **(c)** **(d)**

Figure 11. Pressure contour distribution of minibuses' front views at 27.7 m/s **(a)**T1- **(b)**T2 **(c)**T3-**(d)**T4

Figure 12 shows the side-view pressure distribution of the minibus models at 27.7 m/s. The T1 configuration exhibits a strong pressure gradient between the frontal stagnation zone and the low-pressure wake, indicating substantial pressure-induced drag generation. In the T2 model, streamlined pressure recovery along the side surfaces mitigates boundary layer separation, contributing to a more compact and stable wake region. The pronounced rear suction zones in T3 and T4 suggest earlier flow detachment and increased form drag due to inefficient pressure recovery. Collectively, the pressure contour patterns validate the aerodynamic advantage of the T2 model, as its smoother gradients and reduced wake suggest superior flow control.

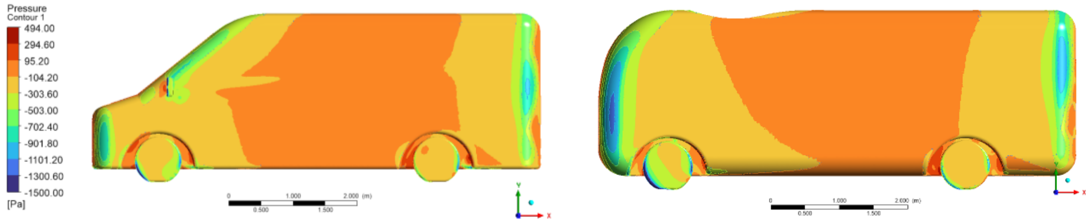

(a) **(c)**

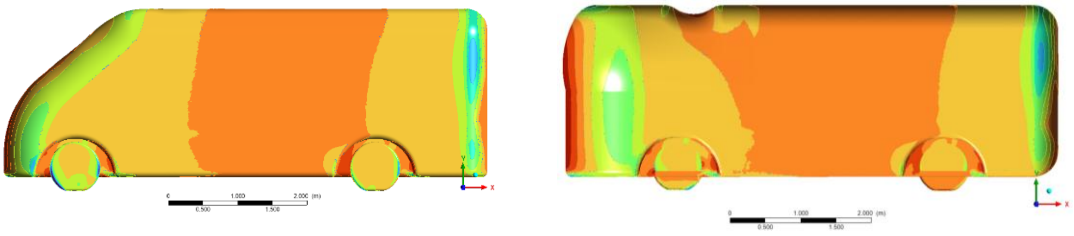

(b) (d)

Figure 12. Pressure contour distribution of 27.7 m/s in the mid-plane of the side views of minibuses **(a)**T1- **(b)**T2- **(c)**T3- **(d)**T4

Figure 13 illustrates the streamlines around the minibus models at 27.7 m/s along the mid-plane (Z = 0). The wake of the T1 model features disorganized and expansive vortex structures, signifying premature flow separation and elevated aerodynamic resistance. The T2 configuration produces a narrower, coherent wake structure, indicating postponed boundary layer detachment and enhanced flow stability along the vehicle contour, resulting in lower drag. Earlier onset of separation in T3 and T4 leads to the development of wider turbulent wakes, which contribute to increased energy dissipation and drag penalties. Overall, the T2 model exhibits the most aerodynamically efficient flow pattern, characterized by attached streamlines and a compact wake—hallmarks of low-drag configurations.

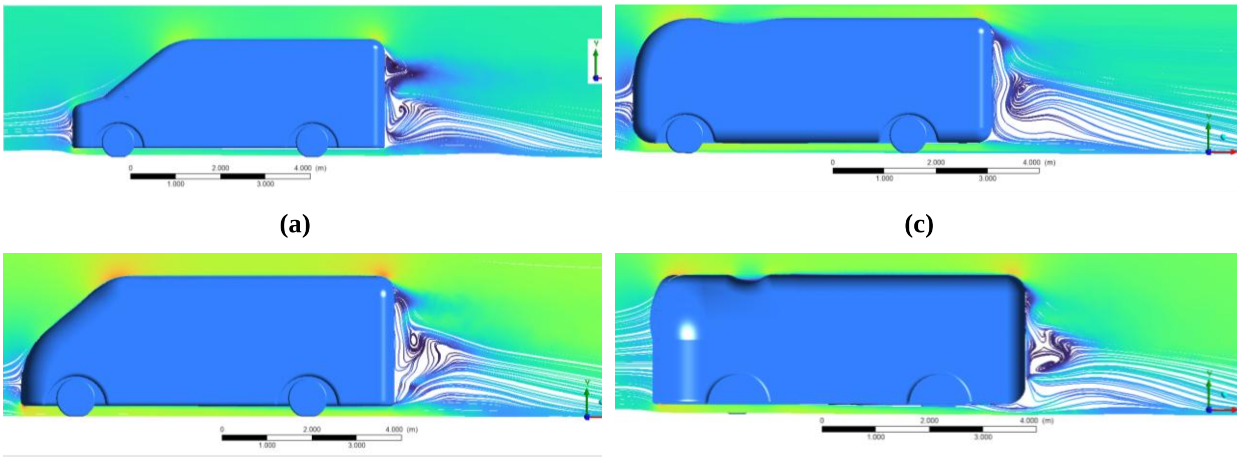

(a) (c)

(b) (d)

Figure 13. Streamlines around the models at 27.7 m/s on the mid-plane (Z = 0). **(a)**T1- **(b)**T2 **(c)**T3-**(d)**T4

Flow separation begins just after the roofline in T1, resulting in a wide turbulent wake. In contrast, T2 delays this separation, forming a narrower low-velocity region. T3 and T4 experience earlier detachment, leading to larger separated flow zones and greater drag.

4.4. Experimental Validation of CFD Results

Experimental tests for the 1:28 scaled T2 prototype were performed in the closed-circuit wind tunnel facility at the Department of Mechanical Engineering, Celal Bayar University. The tunnel provides airflow up to 70 m/s and features a test section of 0.300×0.300 m² with a length of 1 m. The best-performing T2 configuration was geometrically downscaled by a factor of 1:28, preserving geometric, kinematic, and dynamic similarity to ensure valid extrapolation to full-scale behavior.

The physical appearance of the prototype and its placement in the wind tunnel test section are shown in Figure 14 (a) and (b), respectively.

(a) **(b)**

Figure 14. (a) 1:28 scaled T2 prototype **(b)** The 1:28 scaled T2 prototype positioned inside the test section of the low-speed open-circuit wind tunnel during experimental setup.

Dynamic similarity was enforced by equating the Reynolds numbers between the prototype and full-scale model, following the relation Vm·Lm = Vp·Lp, a standard in scaled aerodynamic modeling. While the full-scale model had a characteristic length Lm=6.961 m, the scaled model's length was calculated as Lp=0.248 m, Given a freestream velocity of Vp=27.7 m/s in CFD analysis, the corresponding wind tunnel velocity Vm was determined as 1 m/s, ensuring equal Reynolds numbers. The frontal area of the 1:1 T2 model was 4.8 m², which was reduced to 0.006 m² in the scaled prototype. Boundary conditions in the experiment were defined with no-slip walls and a moving ground to match CFD settings and flow behavior. Experimental results showed strong agreement with numerical simulations in terms of drag coefficient. Table 3 confirms that dynamic similarity was successfully maintained and that the drag coefficients of both scales closely matched.

Table 3. Numerical results for T2 Model at equal Reynolds number for 1:1 scale and 1:28 scale model

Model	Re	Velocity (m/s)	Cd (Drag Coefficient)	Fd (N)
T2 (1:1)	3.85E+05	1	0.346	1.028
T2 (1:28)	3.85E+05	27.7	0.356	1.004

Three separate wind tunnel experiments were conducted on the 1:28 scaled T2 model at a flow velocity of 27.7 m/s to determine the drag coefficient and total drag force. The CFD and wind tunnel results for both the 1:1 and 1:28 scale T2 models—matched via Reynolds number equivalence exhibited strong correlation, validating the accuracy of the numerical predictions. The difference between the drag coefficients obtained from CFD and wind tunnel tests for the 1:28 scaled T2 model was calculated as 11.4%. This difference falls within the acceptable range reported in the literature for aerodynamic validation studies, where deviations of 5–15% are commonly observed due to the inherent differences between physical experiments and idealized numerical models [57, 16, 63, 64]. Figure 4.7 shows the comparison of drag force and drag coefficient values obtained from experimental wind tunnel tests and numerical CFD analyses for the 1:28 scaled T2 model at a flow velocity of 27.7 m/s. The results indicate a close agreement between both methods. The experimental drag force was measured as 1.12 N and the numerical result was 1.004 N. Similarly, the drag coefficient values were 0.399 and 0.356, respectively.

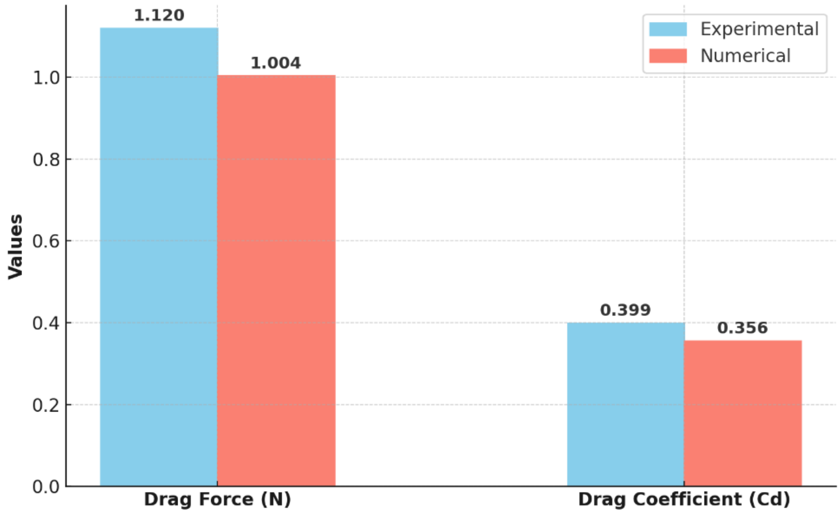

Figure 15. Experimental vs Numerical Drag Data for the T2 Model at 27.7 m/s

When examining the drag coefficients, the difference between experimental and numerical values was calculated to be approximately 11.4%. Similarly, the difference in total drag force between the experimental and numerical results was found to be about 10.36%. This level of agreement reinforces the reliability of the CFD setup and confirms its suitability for evaluating biomimetic vehicle geometries. Similar studies in the literature report acceptable deviation ranges between 5–15% depending on model complexity, turbulence assumptions, and scale effects [16.63,64]. In addition, the blockage ratio of the test setup was calculated as 7%, which is below the widely accepted critical threshold of 7.5% for low-speed wind tunnel experiments [61]. The significant reduction in drag achieved through biomimetic design not only enhances aerodynamic performance but also leads to measurable improvements in energy efficiency and environmental sustainability. For instance, a 16.03% reduction in drag coefficient may yield an approximate 8% reduction in fuel consumption at highway speeds [18].

5. CONCLUSION

This study investigated the aerodynamic effects of biomimetic minibus designs inspired by aquatic species with prominent head structures and agile body forms—specifically the humphead wrasse (T2), green humphead parrotfish (T3), and flowerhorn fish (T4). Among the developed designs, the T2 model inspired by the humphead wrasse exhibited the best aerodynamic performance, achieving a 16.03% reduction in drag coefficient compared to the reference model. The T3 and T4 models also showed notable improvements in flow structure and drag characteristics. Experimental validation of the 1:28 scaled T2 model supported the CFD results, with a drag coefficient deviation of 11.4% and a drag force difference of 10.3% both within acceptable ranges. Pressure and streamline visualizations revealed more stable and attached flow patterns around the biomimetic models. These aerodynamic improvements are directly linked to energy efficiency: A 16.03% reduction in drag coefficient can translate into approximately 8% fuel savings at highway speeds. For a commercial minibus driving 45,000 km per year, this corresponds to a saving of about 324 liters of fuel annually, which further results in a carbon emission reduction of approximately 748 kg CO_2 per year.

In future studies, incorporating dynamic effects such as crosswind sensitivity, rotating wheels, and unsteady flow behavior could provide more comprehensive insight. Optimization techniques may also be applied to refine the geometry further, combining aerodynamic performance with practical design constraints. Exploring structural durability and manufacturability of such biomimetic forms would enhance their feasibility for commercial vehicle applications.

NOMENCLATURE

Nomenclature

English Letters

Cd	Drag coefficient
Fd	Drag Force (N)
g	Gravity (m/s^2)
P	Pressure (Pa)
Vp	Velocity of prototype (m/s)
Vm	Velocity of model (m/s)
Lp	Length of prototype (m)
Lm	Length of model (m)

x, y, z — Cartesian coordinate indices

Greek Letters

μ	Dynamic viscosity (kg/ms)
ν	Kinematic viscosity (m²/s)
U*	Friction velocity (m/s)
τ_{ω}	Wall shear stress (Pa)
δ	Displacement thickness (m)
θ	Momentum thickness (m)

CFD	Computational Fluid Dynamics
DNS	Direct Numerical Simulation
LES	Large Eddy Simulation
RANS	Reynolds-Averaged Navier–Stokes
URANS	Unsteady Reynolds-Averaged Navier–Stokes
SIMPLE	Semi-Implicit Method for Pressure-Linked Equations
PISO	Pressure-Implicit with Splitting of Operators

DECLARATION OF ETHICAL STANDARDS

The authors of the paper submitted declare that nothing which is necessary for achieving the paper requires ethical committee and/or legal-special permissions.

CONTRIBUTION OF THE AUTHORS

Erman Doğan: Performed the experiments and analysed the results.

Seda Kırmacı Arabacı: Conceived and supervised the research, contributed to the methodology, and critically revised the manuscript.

CONFLICT OF INTEREST

There is no conflict of interest in this study.

REFERENCES

[1] Wijegunawardana ID, de Mel WR. Biomimetic designs for automobile engineering: A review. International Journal of Automotive and Mechanical Engineering 2021; 18: 9029-9041.

[2] Benyus JM. Biomimicry: Innovation inspired by nature. Perennial, New York, US, 2002.

[3] Van Wassenbergh S, Van Manen K, Marcroft TA, Alfaro ME, Stamhuis EJ. Boxfish swimming paradox resolved: Forces by the flow of water around the body promote manoeuvrability. Journal of the Royal Society Interface 2015; 12(103): 20141146.

[4] Airbus. Biomimicry: Imitating nature's best-kept secrets. Airbus. https://www.airbus.com/en/innovation/disruptive-concepts/biomimicry Access date: 15 February 2025.

[5] Muthuramalingam M, Puckert DK, Rist U, Bruecker C. Transition delay using biomimetic fish scale arrays. Scientific Reports 2020; 10: 14534.

[6] Muthuramalingam M, Villemin LS, Bruecker C. Streak formation in flow over biomimetic fish scale arrays. Journal of Experimental Biology 2019; 222: jeb205963.

[7] EarthSky. A kingfisher inspired a bullet train. EarthSky. https://earthsky.org/earth/sunni-robertson-on-how-a-kingfisher-inspired-a-bullet-train/ Access date: 15 February 2025.

[8] Turner JS, Soar RC. Beyond biomimicry: What termites can tell us about realizing the living building. Proceedings of the First International Conference on Industrialized Intelligent Construction (I3CON), Loughborough University, Loughborough, UK, 2008.

[9] Swim-Swam SSPC. Why is the Speedo Fastskin based on shark skin. Swim-Swam. https://swimswam.com/sspc-why-is-the-speedo-fastskin-based-on-shark-skin/ Access date: 15 February 2025.

[10] Morales AT, Tamayo Fajardo JA, González-García H. High-speed swimsuits and their historical development in competitive swimming. Frontiers in Psychology 2019; 10: 2639.

[11] Yan YY. Recent advances in computational simulation of macro, meso and micro-scale biomimetics related fluid flow problems. Journal of Bionic Engineering 2007; 4(2): 97-107.

[12] Fish FE, Weber PW, Murray MM, Howle LE. The tubercles on humpback whales' flippers: Application of bio-inspired technology. Integrative and Comparative Biology 2011; 51(1): 203-213.

[13] Mercedes Benz. Mercedes Benz media document. Mercedes Benz. https://mercedes-benz-media.co.uk/assets/documents/original/5971-064759700_1218104423.doc Access date: 15 February 2025.

[14] Chowdhury H, Islam R, Hussein M, Zaid M, Loganathan B, Alam F. Design of an energy efficient car by biomimicry of a boxfish. Energy Procedia 2019; 160: 40-44.

[15] Peng S, Liu X, Li Z, Jiang F. Application of bionics of tiger beetle to aerodynamic optimization of MIRA fastback model. DEStech Transactions on Computer Science and Engineering 2018.

[16] Arabacı SK, Pakdemirli M. Aerodynamic improvements of buses inspired by beluga whales. Journal of Applied Fluid Mechanics 2023; 16(12): 2569-2580.

[17] Chowdhury H, Loganathan B, Ahmed T, Mustary I, Sonyy SM, Alam F. Aerodynamic design of an energy-efficient light truck by biomimicry. AIP Conference Proceedings 2022; 2681: 020101.

[18] Kim JJ, Hong J, Lee SJ. Bio-inspired cab-roof fairing of heavy vehicles for enhancing drag reduction and driving stability. International Journal of Mechanical Sciences 2017; 131-132: 868-879.

[19] Ghaffar H, Yusoff H, Ibrahim D, Budin S, Razak MRA. A simulation study of tubercles effect of aerodynamics performance on car rear spoiler. Journal of Physics: Conference Series 2019; 1349: 3-9.

[20] Fish FE. Biomimetics: Determining engineering opportunities from nature. Proceedings of the SPIE NanoScience + Engineering, San Diego, CA, US, 2009.

[21] Venegas I, Oñate A, Pierart FG, Valenzuela M, Narayan S, Tuninetti V. Efficient mako shark-inspired aerodynamic design for concept car bodies in underground road tunnel conditions. Biomimetics 2024; 9: 448.

[22] Kozlov A, Chowdhury H, Mustary I, Loganathan B, Alam F. Bio-inspired design: Aerodynamics of boxfish. Procedia Engineering 2015; 105: 323-328.

[23] Vogel S. Life in moving fluids: The physical biology of flow. Princeton University Press, Princeton, New Jersey, US, 1994.

[24] Domenici P. Habitat, body design and the swimming performance of fish. Vertebrate biomechanics and evolution. BIOS Scientific Publishers Ltd., Oxford, UK, 2003.

[25] Blake RW. Fish functional design and swimming performance. Journal of Fish Biology 2004; 65: 1193-1222.

[26] Fulton CJ, Bellwood DR, Wainwright PC. Wave energy and swimming performance shape coral reef fish assemblages. Proceedings of the Royal Society B 2005; 272: 827-832.

[27] Alben S, Miller LA, Peng J. Efficient kinematics for jet-propelled swimming. Journal of Fluid Mechanics 2013; 733: 100-133.

[28] McLaughlin RL, Grant JWA. Morphological and behavioural differences among brook charr. Environmental Biology of Fishes 1994; 39: 289-300.

[29] Thorsen DH, Westneat MW. Diversity of pectoral fin structure and function in fishes. Journal of Morphology 2005; 263: 133-150.

[30] Fulton CJ, Johansen JL, Steffensen JF. Energetic extremes in aquatic locomotion by coral reef fishes. PLoS ONE 2013; 8: e54033.

[31] Bellwood DR, Wainwright PC. Locomotion in labrid fishes. Coral Reefs 2001; 20: 139-150.

[32] Fulton CJ, Bellwood DR, Wainwright PC. The relationship between swimming ability and habitat use in wrasses. Marine Biology 2001; 139: 25-33.

[33] Wilcox DC. Formulation of the k–ω turbulence model revisited. AIAA Journal 2008; 46(11): 2823-2838.

[34] Camarillo H, Muñoz MM. Weak relationships between swimming morphology and water depth in wrasses and parrotfish. Integrative and Comparative Biology 2020; 60(5): 1309-1319.

[35] Sun L, Liao L, Chen M, Li J, An R. Relation between fish morphological differentiation and pressure drag difference. Ecological Indicators 2023; 156: 111071.

[36] Mohamed EA, Radhwi MN, Abdel Gawad AF. Computational investigation of aerodynamic characteristics of a bus model. American Journal of Aerospace Engineering 2015; 2(1): 64-73.

[37] Ahmad NE, Aboserie E, Gaylard A. Mesh optimization for ground vehicle aerodynamics. CFD Letters 2010; 2(1): 54-65.

[38] Belzile M, Patten J, McAuliffe B, Mayda W, Tanguay B. Review of aerodynamic drag reduction devices for heavy trucks and buses. Technical Report, 2012.

[39] Hu X, Wong T. A numerical study on rear-spoiler of passenger vehicle. World Academy of Science Engineering and Technology 2011; 81: 636-641.

[40] European Automobile Industry Report 2009/2010. European Automobile Manufacturers Association. www.acea.be. Access date: 15 February 2025.

[41] Hucho WH. Aerodynamics of road vehicles. SAE International, USA, 1998.

[42] Peter S, Fiske JHKS. Lean, light and quiet: Advances in automotive energy efficiency through biomimetic design. SAE Technical Paper, SAE International, 2008.

[43] Chateau O, Wantiez L. Site fidelity and activity patterns of a humphead wrasse. Environmental Biology of Fishes 2007; 80(4): 503-508.

[44] Weng KC, Pedersen MW, Del Raye GA, Caselle JE, Gray AE. Umbrella species in marine systems. Endangered Species Research 2015; 27(1): 251-263.

[45] Sadovy Y, Kulbicki M, Labrosse P, Letourneur Y, Lokani P, Donaldson TJ. The humphead wrasse synopsis. Reviews in Fish Biology and Fisheries 2003; 13(3): 327-364.

[46] Froese R, Pauly D. Cheilinus undulatus. FishBase. https://www.fishbase.se/summary/5604 Access date: 15 February 2025.

[47] Chan T, Sadovy Y, Donaldson TJ. Bolbometopon muricatum. IUCN Red List of Threatened Species, 2012.

[48] Froese R, Pauly D. Bolbometopon muricatum. FishBase, 2006.

[49] Datz. The flowerhorn fish. ThinkQuest Library, 2005.

[50] Amphilophus trimaculatus. FishBase. https://www.fishbase.se/summary/4692 Access date: 15 February 2025.

[51] Mercedes-Benz. Sprinter minibüs. Mercedes-Benz. https://www.mercedes-benz.com.tr/vans/tr/sprinter/minibus Access date: 15 February 2025.

[52] Wang Y, Cheng W, Du R, Wang S. Bionic drag reduction for box girders. Energies 2020; 13(17): 4392.

[53] Kücüksariyildiz H, Canli E, Carman K. Aerodynamic drag coefficient of agricultural tractor form. Energy 2024; 296: 131167.

[54] Liao G, Xue M, Yue L, Yang H, Guo P, Hu X, Wang Z, Ma T. Passive drag reduction optimization. Journal of Applied Fluid Mechanics 2025; 18(6): 1639-1651.

[55] Levin J, Chen SH. Aerodynamic of a refrigerated truck. Proceedings of the Institution of Mechanical Engineers Part D 2023.

[56] Kim SH, Kim JJ. Study on drag reduction of commercial vehicle. Journal of the Korean Society of Visualization 2023; 21(2): 8-13.

[57] Farghaly MB, Sarhan HH, Abdelghany ES. Aerodynamic performance enhancement of heavy trucks. CFD Letters 2023; 15(3).

[58] Garcia-Ribeiro D, Bravo-Mosquera PD, Ayala-Zuluaga JA, Martinez-Castañeda DF, Valbuena-Aguilera JS, Cerón-Muñoz HD, Vaca-Rios JJ. Drag reduction of a commercial bus. Proceedings of the Institution of Mechanical Engineers Part D 2023; 237(7): 1623-1636.

[59] Jasak H. Error analysis and estimation for finite volume method with applications to fluid flow. PhD Thesis, Imperial College, London, UK, 1996.

[60] Ferziger JH, Peric M, Street RL. Computational methods for fluid dynamics. Springer Verlag, 2019.

[61] Barlow JB, Rae WH, Pope A. Low-speed wind tunnel testing. John Wiley & Sons, 1999.

[62] Fluent ANSYS. Ansys Fluent 14.5 User's Guide. ANSYS Inc., Canonsburg, PA, US, 2012.

[63] Khalighi B, Zhang S, Koromilas C, Balkanyi SR, Bernal LP, Iaccarino G, Moin P. Unsteady wake flow behind a bluff body. SAE Transactions 2001; 1209-1222.

[64] Srinivas V. Biomimicry as a tool for aerodynamic drag reduction. Intersect: The Stanford Journal of Science, Technology, and Society 2023; 16(3).

[65] Yang CM, Hung JY, Wang YL, Lien YH. Analysis of Mercedes-Benz concept car using biomimicry design. International Journal of Innovation in Management 2019; 7(2): 49-56.

[66] Shams Taleghani A, Torabi F. Recent developments in aerodynamics. Frontiers in Mechanical Engineering 2025; 10: 1537383.

[67] Sareh P. Inspired by nature, refined by numbers: Formal–functional bioinspiration and intelligent computation in vehicle design. Royal Society Open Science 2025; 12(5).